Geophysical Research Letters

Supporting Information for

The importance of ENSO phase during volcanic eruptions for detection and attribution

Flavio Lehner[1], Andrew P. Schurer[2], Gabriele C. Hegerl[2], Clara Deser[1], and Thomas L. Frölicher[3]

[1]Climate Analysis Section, National Center for Atmospheric Research, Boulder, USA

[2]School of Geosciences, University of Edinburgh, Edinburgh, UK

[3]Environmental Physics, Institute of Biogeochemistry and Pollutant Dynamics, ETH Zürich, Switzerland

Content

1 Coincidence of volcanic eruptions and El Niño events in paleoclimate records

Reconstructions of volcanism (Crowley and Unterman 2013) and ENSO (Li et al. 2013) suggest that the coincidence of El Niño events with three consecutive volcanic eruptions of the same or greater magnitude as Agung has not occurred in at least the past 700 years. This was tested by searching for coincidences of eruptions and El Niño events in the same or following year.

2 Alternative observational data sets

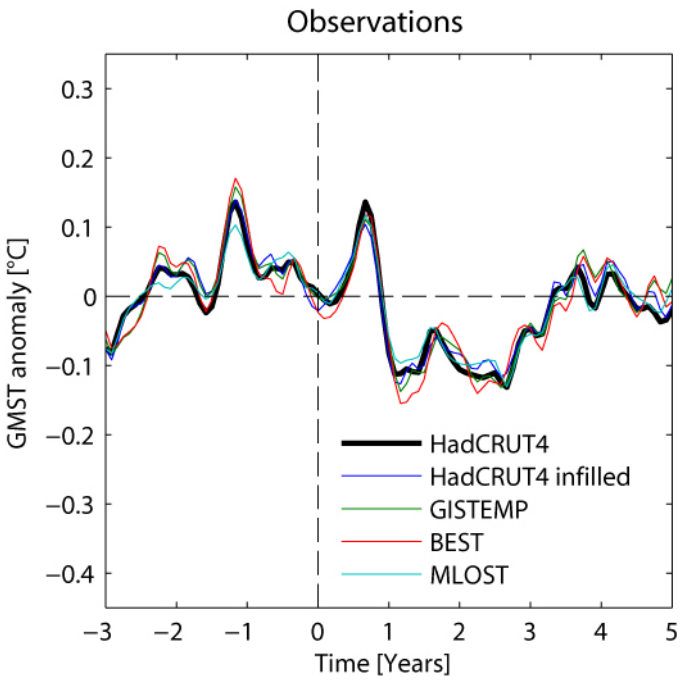

Figure S1: Global mean surface temperature (GMST) anomaly relative to the mean of the 5 years preceding the eruption start date (dashed vertical line) averaged over the three recent volcanic eruptions (Agung, El Chichon and Pinatubo) from different observational data sets. Time series have been smoothed with a triangular 1-2-1 filter for visual purposes only.

3 Detection and attribution extended figure

Figure S2 is an extention of Figure 3 of the main paper. Figure S2b and S2d are identical to Figure 3a and 3b.

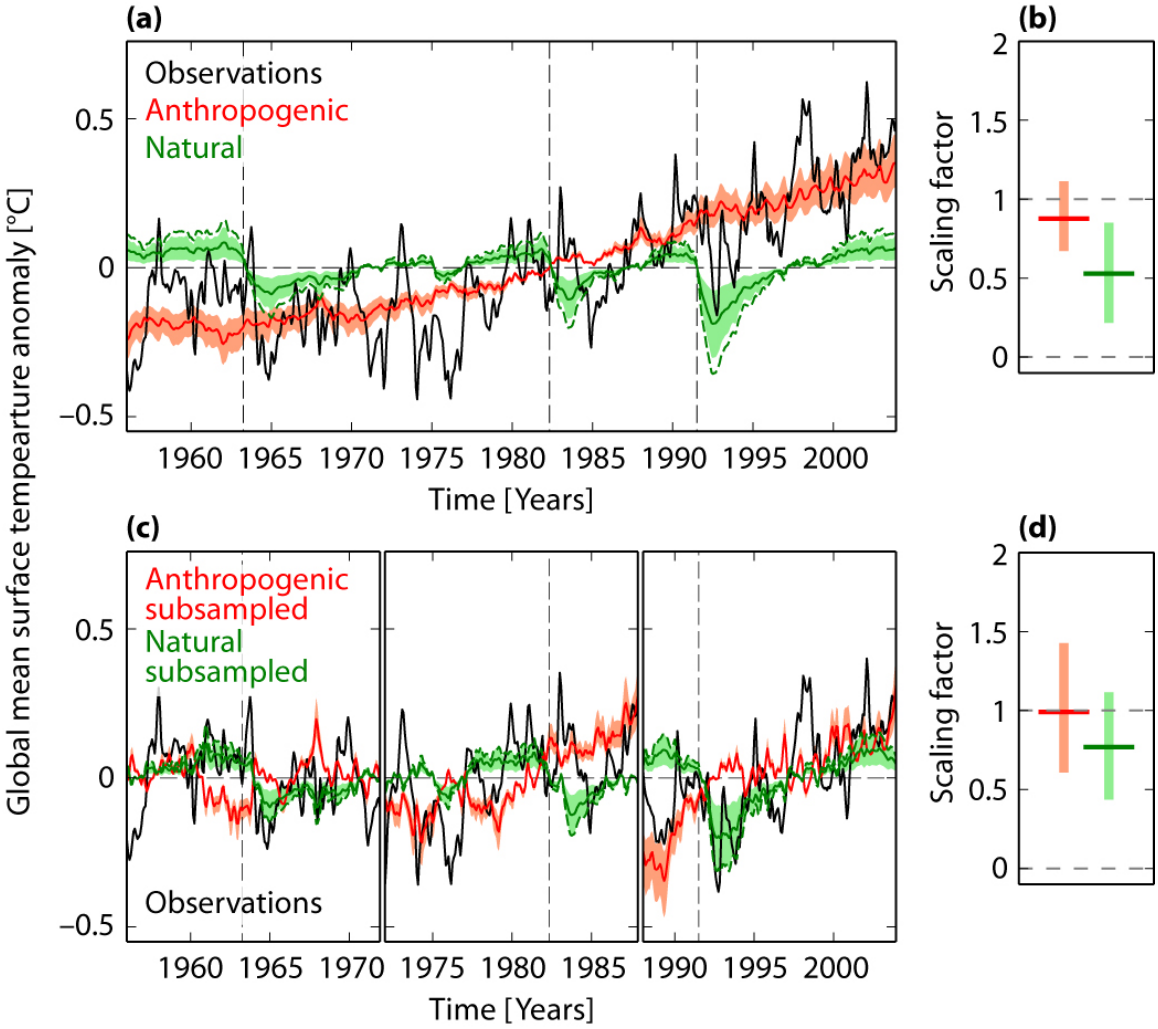

Figure S2: Estimated contribution by natural (green) and anthropogenic (red) forcing to global mean surface temperature anomalies using **(a, b)** all CMIP5 simulations and **(c, d)** only those simulations with the observed ENSO phase. Bold lines are multi-model means multiplied by the best-fit scaling factor. This scaling factor is also plotted as a thick horizontal line in (b) and (d). The shading shows the models multiplied by the 5-95% uncertainty range as plotted by the bar in (b) and (d). Dashed line shows the unscaled model results ('historicalNat' only). Anomalies are taken from the mean of the whole period (a) or the mean of each segment (c). The vertical dashed lines indicate the eruption dates of the three major volcanoes. Time series have been smoothed with a triangular 1-2-1 filter for visual purposes only.

4 Detection and attribution sensitivity analysis

A series of analyses were carried out to test the sensitivity of the results shown in Figure 3 and Figure S2 to the different analysis steps.

Figures S3a and S3f show the best fit scaling factor for the unsampled, continous timeseries as also shown in Figure 3a and 3b in the main paper. They show that the anthropogenic forcing is detectable (values always significantly greater than zero) and consistent with the observations (uncertainty range encompassing one), while the natural forcing is detectable but has a stronger response in models than in the observations (uncertainty range significantly less than zero).

For the final subsampled analysis (Figure S3e and S3j; Figure 3a and 3b in the main paper, respectively) the number of model simulations used to form the multi-model mean and then used in the regression analysis, was limited to 35 'historical' simulations and 13 'historicalNat' simulations. To test the effect of restricting the number of models, Figure S3b and S3g show the range of scaling factors for 100 random combinations of 35 'historical' and 13 'historicalNat' simulations (without splitting the time series into segments yet). As expected, the ranges of the scaling factors show some sensitivity to the subset of models chosen, yet the main conclusions are unchanged from the full set of simulations (compare Figure S3b to S3a and Figure S3g to S3f).

In the final sub-sampled analysis, the GMST time series is split into three equal-length segments. The effect of this on the results for 35 randomly selected 'historical' simulations and 13 randomly selected 'historicalNat' simulations is shown in Figure S3c and S3h. The best-fit anthropogenic scaling factors increase slightly when the time series are split into three segments, likely due to the shortening of the time series. Taking anomalies over three short segments instead of the entire time period decreases the importance of the end points in the regression analysis, in particular if the regression slope has a continuous trend, as is the case for the anthropogenically forced response. For a given segment, this also reduces the signal-to-noise ratio and with that the sensitivity to the choice of randomly selected models. This results in a slightly noisier uncertainty range in Figure S3c and S3h. Importantly for the main conclusions of the study, the scaling factors for the natural forcing response remain unchanged (compare Figure S3g and S3h).

The final sensitivity test addresses the subsampling of the models to select only those with an El Niño event in the boreal winter after each of the large volcanic eruptions. The results are shown in Figure S3d and S3i for 100 different random combinations of the subsampled models (again, for each of the 100 random model combinations we pick 35 from 'historical' and 13 from 'historicalNat'). The best-fit anthropogenic scaling factors are very similar as the ones from the full set of model simulations (compare Figure S3d to S3c). There is less dependence on the choice of model, i.e., the uncertainty range is less noisy, in these subsampled results because there are generally fewer models to choose from due to the

ENSO phase subsampling criteria. The scaling factors for the natural forcing are shown in Figure S3i, in which, crucially, the scaling factor range now always encompasses one, regardless of model selection, while if the models are not sub-sampled (Figure S3f, g, h) the uncertainty range is always significantly less than one. This demonstrates that our conclusions are not a consequence of the model selection.

One final concern regarding the model selection is the large number of simulations in the CMIP5 archive from one particular model family, namely the NASA Goddard Institute for Space Studies (GISS) models: 45 out of 198 'historical' simulations and 20 out of 68 'historicalNat' simulations are from GISS-E2-H-CC, GISS-E2, GISS-E2-R-CC, or GISS-E2-R. We reran the analysis in Figure S3 on the CMIP5 archive excluding all GISS models and found not discernable difference to the results using all CMIP5 models (compare Figure S3 and S4).

The results presented in the main part of the paper are the combination of all the scaling factors calculated for each of the 100 model combinations which are shown in Figure S3d and S3i. These combined ranges are shown in Figure S3e and S3j.

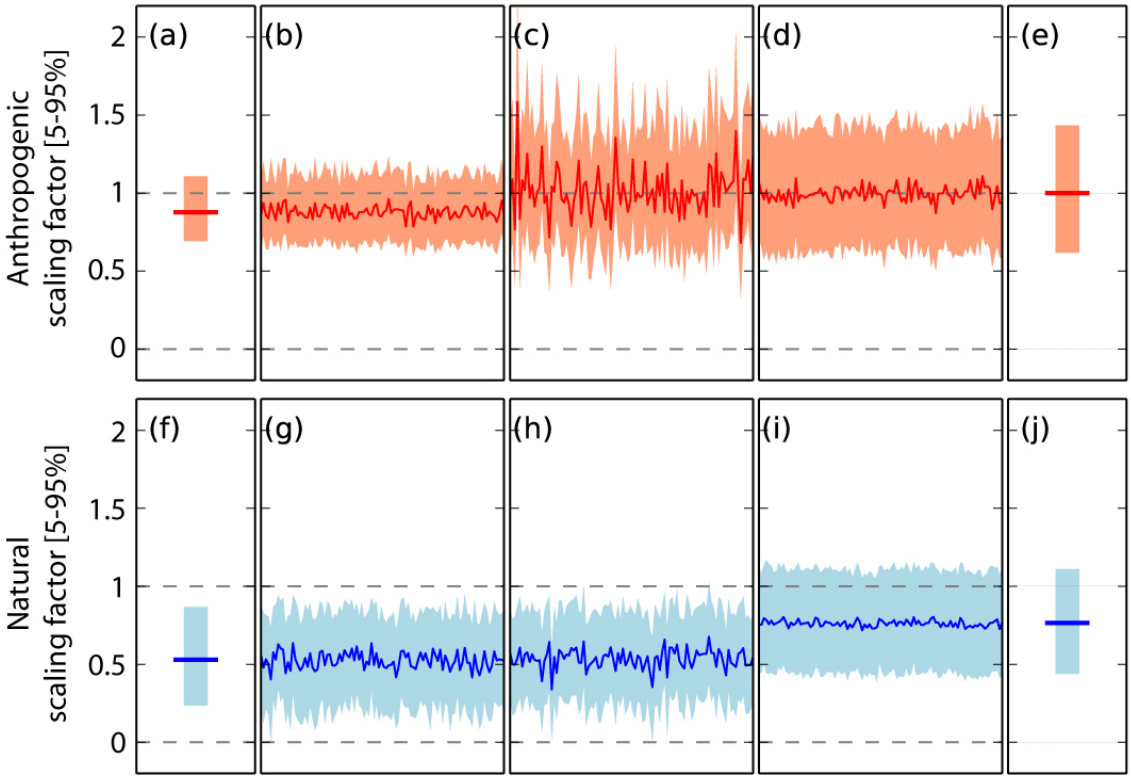

Figure S3: Scaling factors for the response to anthropogenic and natural forcings. **(a)** and **(f)** are based on the continuous timeseries from the unsampled multi-model mean ensembles; **(b)** and **(g)** are based on 100 different combinations of 35 randomly selected 'historical' and 13 'historicalNat' simulations; **(c)** and **(h)** are based on 100 different combinations of 35 randomly selected 'historical' and 13 'historicalNat' simulations split into three segments; **(d)** and **(i)** are based on the same criteria as (c) and (h) but restricted

to those simulations which fulfill the ENSO phase selection criteria. (e) and (j) show the combined results for all model combinations shown in (d) and (i). Color shading indicates the 5-95% range, and the solid curves show the best-fit scaling factor.

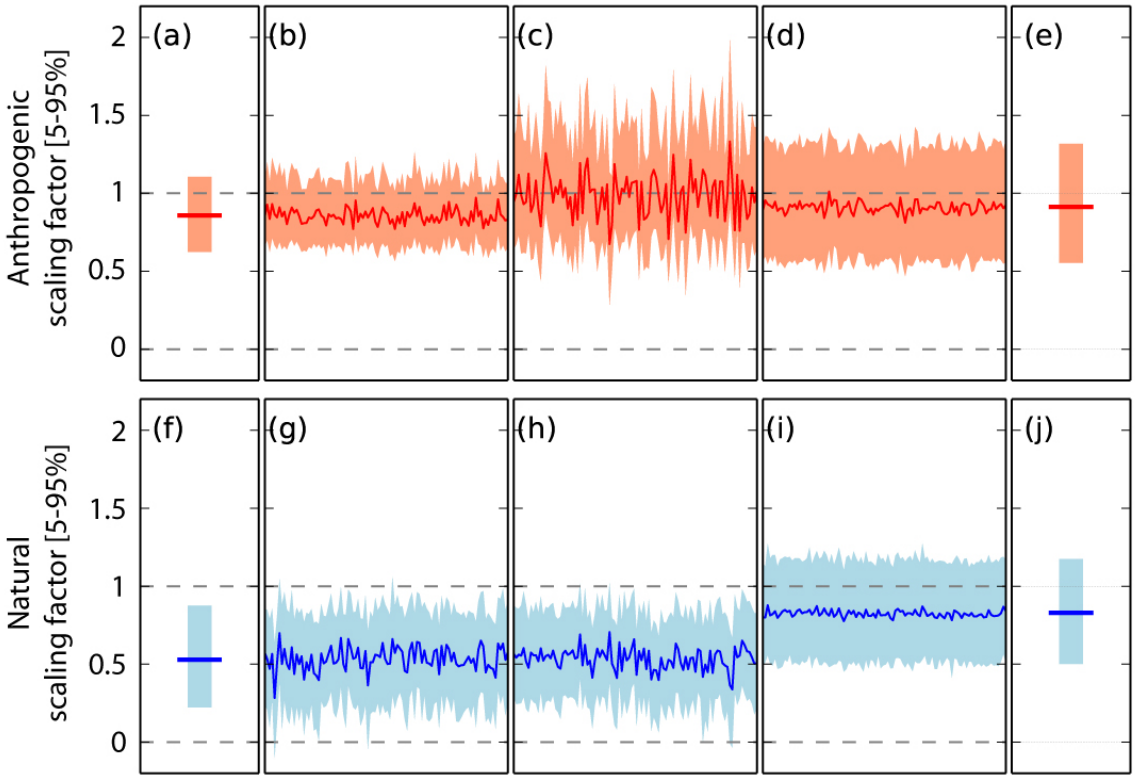

Figure S4: Same as Figure S3, but excluding all GISS models.

5 Uncertainty ranges and control subsampling

To calculate the uncertainty range for the scaling factors, internal variability samples are added to the noise-reduced fingerprints (the multi-model mean from the 'historical' and 'historicalNat' simulations) and observations. For each combination of internal variability samples a scaling factor is calculated. The uncertainty range is then determined from this distribution of scaling factors (see Figure S5a).

To estimate an uncertainty range on the scaling factors of the full CMIP5 model set, 1,000 different combinations of 'piControl' simulation samples are used to calculate a 5-95% range for each of the forcing scaling factors. For the analysis on the subsampled simulations we repeat this procedure 100 times with 1,000 different combinations of 'piControl' simulations. A 5-95% uncertainty range is then calculated from the combination of all 100,000 calculated scaling factors.

Another concern regarding the estimation of an uncertainty range is the question of whether the presence of an El Niño during an eruption systematically changes the character of the internal variability. If so, this might affect the uncertainty range on the scaling factor for natural forcing. The internal variability samples are realizations of the variability around the mean state of a climate in the absence of external forcing. Usually, samples from control simulations (e.g., 'piControl' simulations) are used for this. In the case here, where the model fingerprints have been subsampled to only include those with the observed ENSO phase during post-eruption winters, the internal variability might be different than in the unconstrained case. To investigate this, we subsample the 'piControl' samples in exactly the same way as in the 'historical' and 'historicalNat' simulations (Figure S5b). Unsurprisingly, the global mean surface temperature increases following the three virtual eruptions due to the presence of an El Niño event, which occurs, by definition, in every sample. Crucially though, the variability around the mean is not noticeably different from the unconstrained case, as can be shown by subtracting the multi-model mean time series (Figure S5c). Consequently, in the main paper the uncertainties as derived from the unsampled 'piControl' simulations are used for simplicity.

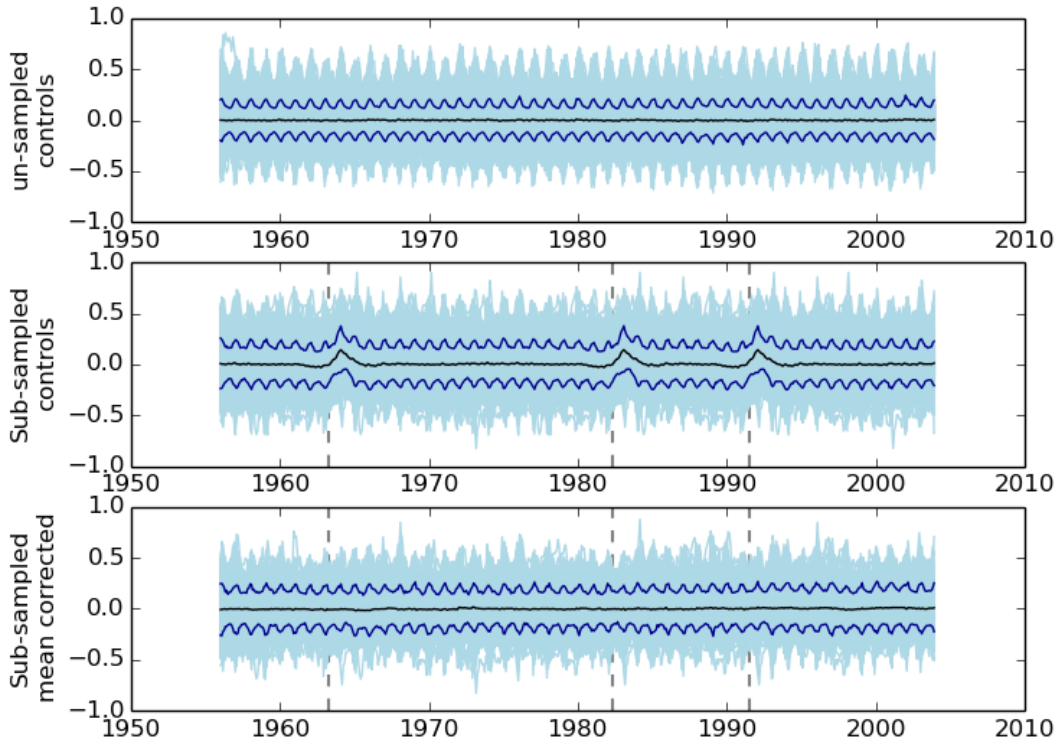

Figure S5: GMST anomalies for different samples of 'piControl' simulations. (a) Unsampled, 'piControl' simulations. (b) 'piControl' simulations subsampled to have an El Niño event in the first virtual post-eruption winter (vertical dashed line). (c) Same as (b) but with the multi-model mean subtracted. No effect in the variability due to subsampling following volcanic eruptions can be seen. Note that the cyclical variability is the seasonal cycle with GMST in boreal winter being more variable than in boreal summer.

6 Results with GFDL models

In addition to the CESM1 Large Ensemble, we investigate the 30-member Geophysical Fluid Dynamics Laboratory (GFDL) ESM2M Large Ensemble, set up in a very similar way as the CESM1 Large Ensemble (Rodgers et al. 2015). The GFDL ESM2M Large Ensemble is initiated in 1950 and also follows the conventional 'historical' forcing protocol of CMIP5. Finally, we investigate a 10-member 'Pacemaker' ensemble with GFDL CM2.1, a GFDL model version that performs very similarly to GFDL-ESM2M (Dunne et al. 2012). This GFDL 'Pacemaker' ensemble was also configured following Kosaka and Xie 2013.

Figure S6 shows results from the GFDL ESM2M free-running 30-member Large Ensemble as well as the 10-member GFDL CM2.1 'Pacemaker' ensemble. The 30-member Large Ensemble has an average cooling of −0.32 °C after volcanic eruptions (measured as the first post-eruption minimum in GMST). By subsampling the simulations according to whether they contain an El Niño in the first winter after an eruption, it can be seen that the volcanic cooling is inhibited by the El Niño, thereby improving the timing of the cooling as compared to observations. However, in almost all of these subsampled simulations there is a strong La Niña 2-3 years after the eruption, unlike observations, leading to an unrealistic cooling of −0.41 °C. This bias is caused by the systematic occurrence of La Niña after an El Niño in this model version (Dunne et al. 2012). Besides being too regular, the ENSO amplitudes are likely too strong in this model, leading to unrealistic amplitudes in GMST. Using instead the GFDL 'Pacemaker' simulations, in which the ENSO chronology matches that in reality, we find that while the pacemaker runs are at the upper end of the entire model distribution, the model still overestimates the post-eruption cooling, indicating that it may indeed have an overly strong response to volcanic forcing and that the discrepancy with observations cannot be fully explained by the ENSO phase sampling. Investigating the reasons for this overestimated cooling in the GFDL models is beyond the scope of this study.

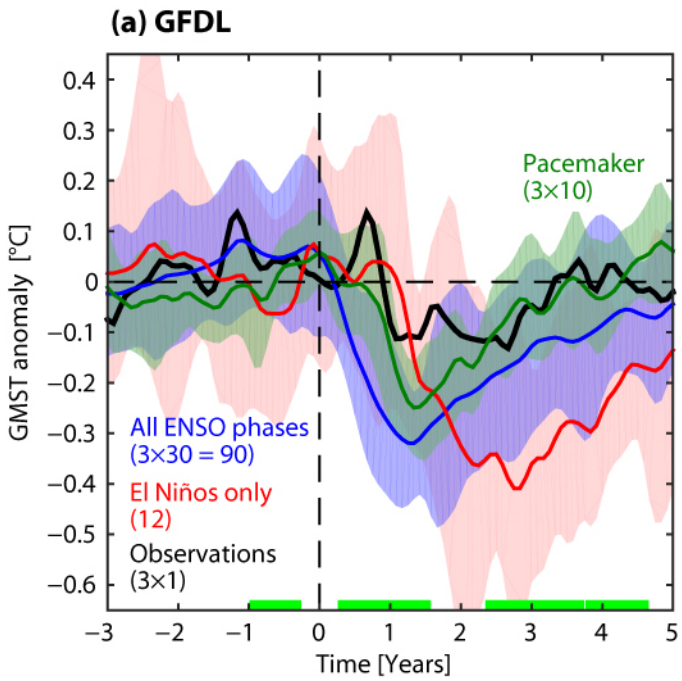

Figure S6: Observed and simulated global mean surface temperature (GMST) anomaly relative to the mean of the 5 years preceding the eruption start date (dashed vertical line) averaged over the three recent volcanic eruptions (Agung, El Chichon and Pinatubo). (a) GFDL-ESM2M large ensemble and 'Pacemaker' simulations. The average over 3 eruptions is shown (see text for details). The colored shading gives the 5-95% confidence interval. The number of ensemble members considered is given in brackets. The months during which the blue and red curves are significantly different (t-test, 95% confidence) are indicated in bright green along the x-axis. Time series have been smoothed with a triangular 1-2-1 filter for visual purposes only.

7 Additional figure for CESM1 'Pacemaker' simulations

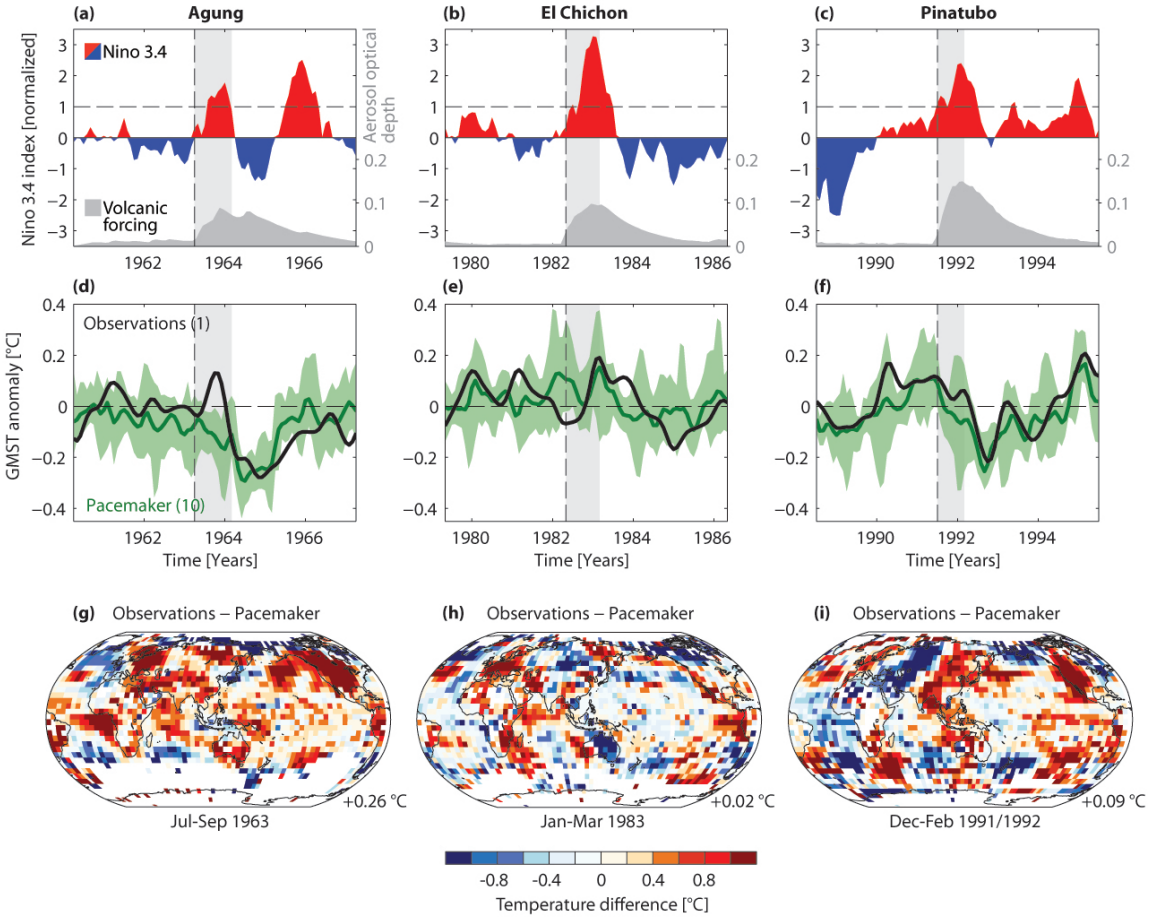

Figure S7: CESM1 'Pacemaker' results for the individual eruptions of **(a, d, g)** Agung, **(b, e, h)** El Chichon, and **(c, f, i)** Pinatubo. **(Top row)** Same as Figure 1. **(Middle row)** Global mean surface temperature (GMST) response relative to the five years preceding the eruption month from observations (black) and the CESM1 'Pacemaker' simulations (green: shading indicates minimum and maximum across the 10-member 'Pacemaker' ensemble). Time series have been smoothed with a triangular 1-2-1 filter for visual purposes only (one filter iteration for models, and five iterations for observations to make spectral characteristics comparable between models and observations). **(Bottom row)** Temperature difference (observations minus 'Pacemaker' ensemble mean) during a three months period following the eruption start date, centered on the peak positive anomaly in observations. Number in bottom right corner of each map gives the spatial mean of the map, i.e., how much warmer observations are relative to the 'Pacemaker' simulations.

8 Additional figure including the Santa Maria eruption in 1902

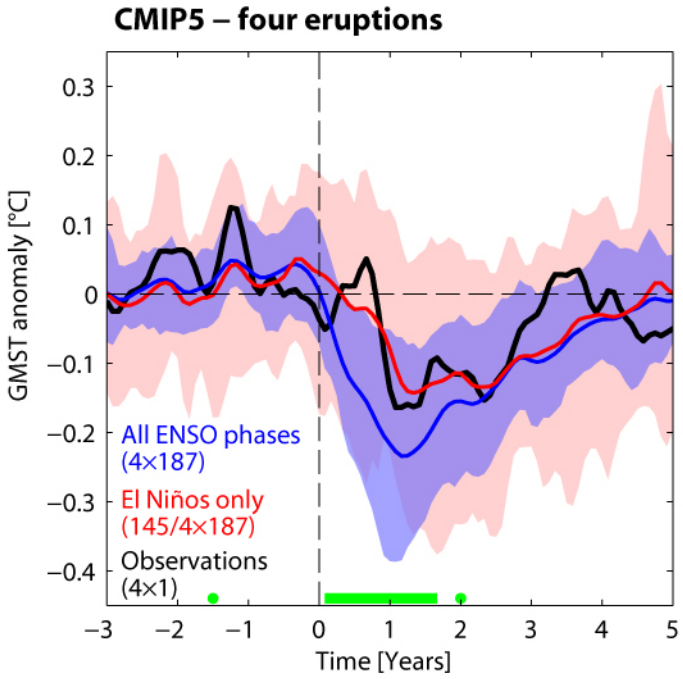

Figure S8: Global mean surface temperature response to the four eruptions of Santa Maria, Agung, El Chichon, and Pinatubo combined. The colored shading gives the 5-95% confidence interval. The number of ensemble members considered is given in brackets. The months during which the blue and red curves are significantly different (t-test, 95% confidence) are indicated in bright green along the x-axis. Time series have been smoothed with a triangular 1-2-1 filter for visual purposes only. Note that the total number of simulations (187) is slightly smaller than in Figure 2 (198), as not all simulations cover 1902.

9 Tables on models, simulations, and subsampling

The number of simulations which meet the ENSO selection criteria for each of the three volcanic eruptions is given in Table S1 (for more details see Tables S2 and S3).

Table S1: Available simulations. Total number of ensemble members available for each experiment **(column 2)** and number of ensemble members that match the observed ENSO state during the boreal winter following the eruption **(columns 3 to 5)**.

Experiment	Number of ensemble members			
	All	Agung	El Chichon	Pinatubo
CMIP5 historical	198	35	55	42
CMIP5 historicalNat	68	17	20	13
CESM1 Large Ensemble	40	9	12	7
GFDL Large Ensemble	30	8	3	1

Table S2: 'historical' simulations used for entire analysis **(column 2)** and those that match the observed ENSO evolution for individual volcanic eruptions **(columns 3 to 5)**. FGOALS-g2 and the CMCC models were excluded, as they do not include volcanic forcing for the historical period.

	Ensemble members historical			
Model	**All**	**Agung**	**El Chichon**	**Pinatubo**
ACCESS1-0	r1i1p1			
ACCESS1-0	r2i1p1			
ACCESS1-0	r3i1p1		r3i1p1	
ACCESS1-3	r1i1p1		r1i1p1	
ACCESS1-3	r2i1p1			
ACCESS1-3	r3i1p1			r3i1p1
bcc-csm1-1	r1i1p1			r1i1p1
bcc-csm1-1	r2i1p1	r2i1p1		
bcc-csm1-1	r3i1p1			r3i1p1
bcc-csm1-1-m	r1i1p1			
bcc-csm1-1-m	r2i1p1	r2i1p1		
bcc-csm1-1-m	r3i1p1			
BNU-ESM	r1i1p1		r1i1p1	r1i1p1
CanESM2	r1i1p1		r1i1p1	
CanESM2	r2i1p1	r2i1p1		
CanESM2	r3i1p1			
CanESM2	r4i1p1			
CanESM2	r5i1p1		r5i1p1	
CCSM4	r1i1p1		r1i1p1	
CCSM4	r1i2p1			

CCSM4	r1i2p2	r1i2p2		
CCSM4	r2i1p1			
CCSM4	r3i1p1			
CCSM4	r4i1p1			
CCSM4	r5i1p1	r5i1p1		
CCSM4	r6i1p1	r6i1p1		
CESM1-BGC	r1i1p1			
CESM1-CAM5	r1i1p1			
CESM1-CAM5	r2i1p1			
CESM1-CAM5	r3i1p1		r3i1p1	
CESM1-CAM5-1-FV2	r1i1p1			
CESM1-CAM5-1-FV2	r2i1p1			
CESM1-CAM5-1-FV2	r3i1p1			r3i1p1
CESM1-CAM5-1-FV2	r4i1p1			
CESM1-FASTCHEM	r1i1p1			
CESM1-FASTCHEM	r2i1p1	r2i1p1		
CESM1-FASTCHEM	r3i1p1			
CESM1-WACCM	r1i1p1	r1i1p1		
CESM1-WACCM	r2i1p1			
CESM1-WACCM	r3i1p1			
CESM1-WACCM	r4i1p1			
CESM1-WACCM	r5i1p1			
CESM1-WACCM	r6i1p1		r6i1p1	
CESM1-WACCM	r7i1p1			
CNRM-CM5	r10i1p1	r10i1p1		
CNRM-CM5	r1i1p1			
CNRM-CM5	r2i1p1		r2i1p1	
CNRM-CM5	r3i1p1	r3i1p1	r3i1p1	r3i1p1
CNRM-CM5	r4i1p1			
CNRM-CM5	r5i1p1	r5i1p1	r5i1p1	r5i1p1
CNRM-CM5	r6i1p1			
CNRM-CM5	r7i1p1		r7i1p1	
CNRM-CM5	r8i1p1	r8i1p1		r8i1p1
CNRM-CM5	r9i1p1			
CNRM-CM5-2	r1i1p1		r1i1p1	
CSIRO-Mk3-6-0	r10i1p1			
CSIRO-Mk3-6-0	r1i1p1			
CSIRO-Mk3-6-0	r2i1p1		r2i1p1	r2i1p1
CSIRO-Mk3-6-0	r3i1p1		r3i1p1	
CSIRO-Mk3-6-0	r4i1p1		r4i1p1	r4i1p1
CSIRO-Mk3-6-0	r5i1p1			

CSIRO-Mk3-6-0	r6i1p1			
CSIRO-Mk3-6-0	r7i1p1			
CSIRO-Mk3-6-0	r8i1p1	r8i1p1		
CSIRO-Mk3-6-0	r9i1p1			
CSIRO-Mk3L-1-2	r1i2p1			
CSIRO-Mk3L-1-2	r2i2p1			r2i2p1
CSIRO-Mk3L-1-2	r3i2p1	r3i2p1		
EC-EARTH	r12i1p1		r12i1p1	
EC-EARTH	r1i1p1			
EC-EARTH	r2i1p1			
EC-EARTH	r6i1p1			r6i1p1
EC-EARTH	r8i1p1			r8i1p1
EC-EARTH	r9i1p1			
FIO-ESM	r1i1p1			
FIO-ESM	r2i1p1	r2i1p1		
FIO-ESM	r3i1p1	r3i1p1		r3i1p1
GFDL-CM2p1	r10i1p1			
GFDL-CM2p1	r1i1p1			
GFDL-CM2p1	r2i1p1			
GFDL-CM2p1	r3i1p1		r3i1p1	
GFDL-CM2p1	r4i1p1		r4i1p1	r4i1p1
GFDL-CM2p1	r5i1p1			
GFDL-CM2p1	r6i1p1			
GFDL-CM2p1	r7i1p1			
GFDL-CM2p1	r8i1p1			
GFDL-CM2p1	r9i1p1			r9i1p1
GFDL-CM3	r1i1p1			
GFDL-CM3	r2i1p1			
GFDL-CM3	r3i1p1		r3i1p1	
GFDL-CM3	r4i1p1	r4i1p1	r4i1p1	
GFDL-CM3	r5i1p1			r5i1p1
GFDL-ESM2G	r1i1p1			
GFDL-ESM2M	r1i1p1		r1i1p1	r1i1p1
GISS-E2-H	r1i1p1			
GISS-E2-H	r1i1p2			r1i1p2
GISS-E2-H	r1i1p3		r1i1p3	r1i1p3
GISS-E2-H	r2i1p1			
GISS-E2-H	r2i1p2		r2i1p2	
GISS-E2-H	r2i1p3			
GISS-E2-H	r3i1p1			
GISS-E2-H	r3i1p2		r3i1p2	

GISS-E2-H	r3i1p3			
GISS-E2-H	r4i1p1			
GISS-E2-H	r4i1p2			
GISS-E2-H	r4i1p3		r4i1p3	
GISS-E2-H	r5i1p1		r5i1p1	
GISS-E2-H	r5i1p2			
GISS-E2-H	r5i1p3			
GISS-E2-H	r6i1p1			r6i1p1
GISS-E2-H	r6i1p2			
GISS-E2-H	r6i1p3			r6i1p3
GISS-E2-H-CC	r1i1p1	r1i1p1	r1i1p1	
GISS-E2-R	r1i1p1			
GISS-E2-R	r1i1p121			
GISS-E2-R	r1i1p122			
GISS-E2-R	r1i1p124	r1i1p124	r1i1p124	
GISS-E2-R	r1i1p125		r1i1p125	
GISS-E2-R	r1i1p126			
GISS-E2-R	r1i1p127	r1i1p127		
GISS-E2-R	r1i1p128	r1i1p128		
GISS-E2-R	r1i1p2			
GISS-E2-R	r1i1p3			
GISS-E2-R	r2i1p1			
GISS-E2-R	r2i1p2			r2i1p2
GISS-E2-R	r2i1p3		r2i1p3	
GISS-E2-R	r3i1p1		r3i1p1	r3i1p1
GISS-E2-R	r3i1p2		r3i1p2	
GISS-E2-R	r3i1p3	r3i1p3		
GISS-E2-R	r4i1p1			r4i1p1
GISS-E2-R	r4i1p2	r4i1p2		
GISS-E2-R	r4i1p3			
GISS-E2-R	r5i1p1			
GISS-E2-R	r5i1p2			r5i1p2
GISS-E2-R	r5i1p3			
GISS-E2-R	r6i1p1		r6i1p1	
GISS-E2-R	r6i1p2		r6i1p2	

GISS-E2-R	r6i1p3		r6i1p3	
GISS-E2-R-CC	r1i1p1		r1i1p1	
HadCM3	r10i1p1			r10i1p1
HadCM3	r1i1p1			
HadCM3	r2i1p1			
HadCM3	r3i1p1			
HadCM3	r4i1p1	r4i1p1		
HadCM3	r5i1p1	r5i1p1	r5i1p1	
HadCM3	r6i1p1			
HadCM3	r7i1p1		r7i1p1	r7i1p1
HadCM3	r8i1p1	r8i1p1	r8i1p1	r8i1p1
HadCM3	r9i1p1		r9i1p1	r9i1p1
HadGEM2-AO	r1i1p1			
HadGEM2-CC	r1i1p1	r1i1p1		
HadGEM2-ES	r1i1p1			
HadGEM2-ES	r2i1p1			
HadGEM2-ES	r3i1p1		r3i1p1	
HadGEM2-ES	r4i1p1		r4i1p1	
HadGEM2-ES	r5i1p1			
inmcm4	r1i1p1			r1i1p1
IPSL-CM5A-LR	r1i1p1	r1i1p1	r1i1p1	
IPSL-CM5A-LR	r2i1p1			r2i1p1
IPSL-CM5A-LR	r3i1p1		r3i1p1	
IPSL-CM5A-LR	r4i1p1			
IPSL-CM5A-LR	r5i1p1		r5i1p1	
IPSL-CM5A-LR	r6i1p1	r6i1p1		
IPSL-CM5A-MR	r1i1p1		r1i1p1	
IPSL-CM5A-MR	r2i1p1			r2i1p1
IPSL-CM5A-MR	r3i1p1			
IPSL-CM5B-LR	r1i1p1			
MIROC4h	r1i1p1			r1i1p1
MIROC4h	r2i1p1	r2i1p1		
MIROC4h	r3i1p1			
MIROC5	r1i1p1			
MIROC5	r2i1p1			
MIROC5	r3i1p1		r3i1p1	
MIROC5	r4i1p1			
MIROC5	r5i1p1			
MIROC-ESM	r1i1p1			
MIROC-ESM	r2i1p1			
MIROC-ESM	r3i1p1		r3i1p1	r3i1p1

MIROC-ESM-CHEM	r1i1p1			
MPI-ESM-LR	r1i1p1	r1i1p1		
MPI-ESM-LR	r2i1p1			
MPI-ESM-LR	r3i1p1		r3i1p1	
MPI-ESM-MR	r1i1p1			
MPI-ESM-MR	r2i1p1			r2i1p1
MPI-ESM-MR	r3i1p1		r3i1p1	
MPI-ESM-P	r1i1p1	r1i1p1		r1i1p1
MPI-ESM-P	r2i1p1			r2i1p1
MRI-CGCM3	r1i1p1	r1i1p1		r1i1p1
MRI-CGCM3	r2i1p1	r2i1p1		r2i1p1
MRI-CGCM3	r3i1p1			r3i1p1
MRI-CGCM3	r4i1p2			
MRI-CGCM3	r5i1p2		r5i1p2	
MRI-ESM1	r1i1p1			r1i1p1
NorESM1-M	r1i1p1			
NorESM1-M	r2i1p1		r2i1p1	
NorESM1-M	r3i1p1		r3i1p1	
NorESM1-ME	r1i1p1	r1i1p1		
NorESM1-ME	r1i1p2		r1i1p2	
Total number	**198**	**35**	**55**	**42**

Table S3: historicalNat simulations used for entire analysis **(column 2)** and those that match the observed ENSO evolution for individual volcanic eruptions **(columns 3 to 5)**.

	Ensemble members historicalNat			
Model	**All**	**Agung**	**El Chichon**	**Pinatubo**
bcc-csm1-1	r1i1p1			
BNU-ESM	r1i1p1			
CanESM2	r1i1p1		r1i1p1	
CanESM2	r2i1p1	r2i1p1	r2i1p1	
CanESM2	r3i1p1	r3i1p1	r3i1p1	
CanESM2	r4i1p1		r4i1p1	r4i1p1
CanESM2	r5i1p1		r5i1p1	
CCSM4	r1i1p1			
CCSM4	r2i1p1	r2i1p1		
CCSM4	r4i1p1			
CCSM4	r6i1p1			r6i1p1
CESM1-CAM5	r1i1p1			
CESM1-CAM5	r2i1p1		r2i1p1	

CESM1-CAM5	r3i1p1			
CESM1-CAM5-1-FV2	r1i1p1	r1i1p1		
CESM1-CAM5-1-FV2	r3i1p1	r3i1p1		
CESM1-CAM5-1-FV2	r4i1p1			
CNRM-CM5	r1i1p1			
CNRM-CM5	r2i1p1	r2i1p1		r2i1p1
CNRM-CM5	r3i1p1			
CNRM-CM5	r4i1p1		r4i1p1	
CNRM-CM5	r5i1p1			
CNRM-CM5	r8i1p1			
CSIRO-Mk3-6-0	r1i1p1			
CSIRO-Mk3-6-0	r2i1p1			r2i1p1
CSIRO-Mk3-6-0	r3i1p1			
CSIRO-Mk3-6-0	r4i1p1			
CSIRO-Mk3-6-0	r5i1p1			
GFDL-CM3	r1i1p1			r1i1p1
GFDL-CM3	r3i1p1	r3i1p1		
GFDL-CM3	r5i1p1			r5i1p1
GFDL-ESM2M	r1i1p1		r1i1p1	
GISS-E2-H	r1i1p1		r1i1p1	
GISS-E2-H	r1i1p3		r1i1p3	r1i1p3
GISS-E2-H	r2i1p1			
GISS-E2-H	r2i1p3		r2i1p3	r2i1p3
GISS-E2-H	r3i1p1		r3i1p1	
GISS-E2-H	r3i1p3	r3i1p3	r3i1p3	
GISS-E2-H	r4i1p1			
GISS-E2-H	r4i1p3			
GISS-E2-H	r5i1p1			
GISS-E2-H	r5i1p3			
GISS-E2-R	r1i1p1	r1i1p1		
GISS-E2-R	r1i1p3	r1i1p3		
GISS-E2-R	r2i1p1			
GISS-E2-R	r2i1p3	r2i1p3		
GISS-E2-R	r3i1p1			
GISS-E2-R	r3i1p3	r3i1p3	r3i1p3	
GISS-E2-R	r4i1p1	r4i1p1		
GISS-E2-R	r4i1p3		r4i1p3	
GISS-E2-R	r5i1p1			
GISS-E2-R	r5i1p3			r5i1p3
HadGEM2-ES	r1i1p1	r1i1p1		
HadGEM2-ES	r2i1p1			

HadGEM2-ES	r3i1p1			r3i1p1
HadGEM2-ES	r4i1p1		r4i1p1	
IPSL-CM5A-LR	r1i1p1			
IPSL-CM5A-LR	r2i1p1	r2i1p1		
IPSL-CM5A-LR	r3i1p1		r3i1p1	r3i1p1
IPSL-CM5A-MR	r1i1p1			r1i1p1
IPSL-CM5A-MR	r2i1p1			
IPSL-CM5A-MR	r3i1p1		r3i1p1	
MIROC-ESM	r1i1p1	r1i1p1		
MIROC-ESM	r2i1p1			
MIROC-ESM	r3i1p1		r3i1p1	
MIROC-ESM-CHEM	r1i1p1		r1i1p1	
MRI-CGCM3	r1i1p1	r1i1p1		
NorESM1-M	r1i1p1			r1i1p1
Total number	**68**	**17**	**20**	**13**

References

Crowley, T. J., and M. B. Unterman, 2013: Technical details concerning development of a 1200 yr proxy index for global volcanism. *Earth Syst. Sci. Data*, **5**, 187–197, doi:10.5194/essd-5-187-2013.

Dunne, J. P., and Coauthors, 2012: GFDL's ESM2 Global Coupled Climate – Carbon Earth System Models. Part I: Physical Formulation and Baseline Simulation Characteristics. *J. Clim.*, **25**, 6646–6665, doi:10.1175/JCLI-D-11-00560.1.

Kosaka, Y., and S.-P. Xie, 2013: Recent global-warming hiatus tied to equatorial Pacific surface cooling. *Nature*, **501**, 403–407, doi:10.1038/nature12534. http://www.ncbi.nlm.nih.gov/pubmed/23995690.

Li, J., and Coauthors, 2013: El Niño modulations over the past seven centuries. *Nat. Clim. Chang.*, **3**, 822–826, doi:10.1038/nclimate1936. http://www.nature.com/doifinder/10.1038/nclimate1936\nhttp://www.nature.com/nclimate/journal/v3/n9/full/nclimate1936.html (Accessed August 10, 2014).

Rodgers, K. B., J. Lin, and T. L. Frölicher, 2015: Emergence of multiple ocean ecosystem drivers in a large ensemble suite with an Earth system model. *Biogeosciences*, **12**, 3301–3320.